Altering microstructure and enhancing mechanical properties during direct energy deposition of Ti-6Al-4V via in-process laser heat treatments

Kouider Abdellah Abdesselam, Steve Gaudez, Steven van Petegem, Veijo Honkimäki, Simon Hallais, Louis Cornet, Maxime Vallet, M V Upadhyay

Altering microstructure and enhancing mechanical properties during direct energy deposition of Ti-6Al-4V via in-process laser heat treatments

K.A. Abdesselam[1], S. Gaudez[1,†], S. Van Petegem[2], V. Honkimäki[3], S. Hallais[1], L. Cornet[4], M. Vallet[4,5], M.V. Upadhyay[1,*]

[1] Laboratoire de Mécanique des Solides (LMS), École Polytechnique, Institut Polytechnique de Paris, CNRS UMR 7649, 91120 Palaiseau, France.
[2] Laboratory for Condensed Matter, PSI, Center for Photon Science, Forschungsstrasse 111, 5232 Villigen PSI, Switzerland.
[3] European Synchrotron Research Facility, Grenoble, France.
[4] Université Paris-Saclay, CentraleSupélec, ENS Paris-Saclay, CNRS, LMPS – Laboratoire de Mécanique Paris-Saclay, 91190 Gif-sur-Yvette, France.
[5] Université Paris-Saclay, CentraleSupélec, CNRS, SMPS – Laboratoire de Structures, Propriétés et Modélisation des Solides, 91190 Gif-sur-Yvette, France.

† Current address: Laboratory for Condensed Matter, PSI, Center for Photon Science, Forschungsstrasse 111, 5232 Villigen PSI, Switzerland.

* Corresponding author e-mail: manas.upadhyay@polytechnique.edu (Manas V. Upadhyay)

Abstract In-process laser-based heat treatment (LHT) is explored as an alternative to post-process heat treatments such as annealing, in order to alter the hcp (α' and α_d) and bcc (β) phase content. Three samples were manufactured with a miniature laser metal deposition machine with the laser operating at 300 W. The reference sample was not subjected to any LHT. For the remaining samples, each deposited layer was subjected to an additional LHT at 100 W (LHT100) for one sample and 300 W (LHT300) for the other, without powder addition. LHT100 showed an overall improvement in the strength/ductility trade-off. Whereas LHT300 resulted in a lower strength but a much higher ductility and toughness than the other samples. Synchrotron X-ray diffraction analysis of as-built samples revealed an insignificant difference between hcp and bcc phase content between different samples. However, scanning electron microscopy uncovered a significant effect of LHTs on the fractions of different hcp phases. Along with the breakdown of α' into α_d and β, evidence of massive transformation from bcc β to hcp α_m was also found in all samples. Results show promising improvement in the material strength/ductility trade-off, demonstrating the potential of in-process LHTs for altering microstructures and tailoring mechanical properties.

Keywords Additive Manufacturing; Ti6Al4V; Phase transformation; Synchrotron X-ray diffraction; Rietveld refinement; Scanning electron microscopy

1 Introduction

Ti-6Al-4V is widely used in different industries such as aerospace, automotive, or medical, due to its high strength-to-weight ratio, high corrosion resistance, and good bio-compatibility [1–5]. In recent years, additive manufacturing (AM) of Ti-6Al-4V has gained importance due to the customization capabilities afforded by the layer-by-layer building approach used in AM as opposed to subtractive or mass-conserving conventional manufacturing techniques. AM of Ti-6Al-4V has been explored using processes such as laser powder bed fusion (LPBF), electron-beam powder bed fusion (EPBF), and laser directed energy deposition (LDED) [6–10] to produce geometrically complex parts that are tailored for a desired application with reduced material waste [6, 11, 12].

For all AM techniques, as-built Ti-6Al-4V exhibits a higher tensile and ultimate strength but poorer ductility in comparison to its conventionally manufactured parts [7, 13]. At the origin of these differences in the mechanical response are the variations in the microstructural (intergranular and intragranular) phenomena, which include the constituent phases, grain sizes and morphology, texture, solid solution, intergranular and intragranular strains, and dislocation density and arrangements.

Ti-6Al-4V exhibits two stable phases: body-centered cubic (bcc) β phase that is stable above the β transus temperature ($\sim$ 980-1000°C [14,15]) and hexagonal close-packed (hcp) α_d below the β transus; the subscript d stands for diffusive. When Ti-6Al-4V is slowly cooled from above the β transus, β transforms diffusively into α_d according to the so-called Burgers orientation relationship (OR): $\{0001\}_\alpha \parallel \{110\}_\beta$ ($\langle 1120\rangle_\alpha \parallel \langle 111\rangle_\beta$). This transformation involves long range atomic diffusion and redistribution of α_d (aluminum, oxygen, carbon and nitrogen) and β (vanadium and iron) stabilizing elements [1,2,16]. The resulting microstructure features lathy and/or globular (more advanced stage of diffusion) α_d separated by thinner laths of β.

When Ti-6Al-4V is processed via AM, which involves rapid cooling rates (10^3 K/s - 10^6 K/s), there is a high propensity for a diffusionless (short-range atomic rearrangement) military phase transformation below the martensitic start temperature ($M_s \sim$ 780-900°C [15,17,18]) of the β phase into the metastable martensitic α' hcp phase exhibiting needle-like (acicular) morphology [6,19]. The so-called military phase transformation involves the shearing of the β phase into the α' phase via a cooperative movement of atoms following the aforementioned Burger's OR [2, 16, 20]. At the time of its formation, α' has the same chemical composition as its parent β phase. Furthermore, the transformation strains and the incoherency in strains at the β-α' interface trigger local plastic deformation that results in a high density of dislocations often observed in AM Ti-6Al-4V [9, 21]. Thus, due to solid solution strengthening and high dislocation density, α' results in high strength in AM Ti-6Al-4V, but at the cost of low ductility [22–24]. However, intrinsic heat treatment due to subsequent addition of layers or post-process annealing can result in the decomposition of α' into α_d and β.

Another metastable phase that could occur due to a diffusionless transformation from β is the so-called massive-α hcp phase, denoted as α_m. In contrast to α' martensite, which forms due to a military transformation, α_m forms via a civilian transformation [16, 25], which involves thermally activated interface migration and growth leading to the formation of irregularly-shaped α_m grains. Similar to α', at the time of nucleation, α_m grains have the same composition as their parent β phase [16, 26]. It is only their irregular shape, which differs significantly from α' and α_d, that allows their identification and segmentation [25, 26]. α_m was first reported to occur at cooling rates greater than 20 K/s and less than 410 K/s from above the β transus by Ahmed et al. [22]. More recently,

Nursyifaulkhair et al. [27] reported that the formation of α_m in LDED Ti-6Al-4V was the highest for cooling rates in between 4000 - 5000 K/s but lesser outside this range; in particular, higher cooling rates resulted in a preferential formation of α'. Since both ranges can occur during all AM processes, the occurrence of α_m can be expected along with α', α_d, and β phases in AM Ti-6Al-4V alloys as reported in recent studies [28–32]. It has also been shown that the solid-state thermal cycling occurring due to layer addition during AM can result in the decomposition of α_m into α_d and β [28–32]. Based on these observations, the current understanding is that α_m exhibits an intermediate strength-ductility response between α' and α_d [32].

In order to achieve a good strength/ductility trade-off of AM Ti-6Al-4V parts, heat treatments such as annealing, solution treatment, aging, tempering, or hot isostatic pressing (HIP) [7, 33–35], are often carried out to alter the microstructure and element distribution primarily through the decomposition of α' into $\alpha_d + \beta$. For example, Sabban et al. [36] were able to achieve a bimodal $\alpha_d + \beta$ globular microstructure on AM Ti-6Al-4V parts improving the ductility by 80% and the toughness by 66% by doing heat treatments over 24h. Li et al. [37] adopted 2h multi-step heat treatments at different temperatures below the β transus leading to a nearly equiaxed microstructure with a good ductility/ultimate tensile strength balance. De Formanoir et al. [38] investigated heat treatments at sub-transus temperature during 2h followed by water quenching to generate an $\alpha' + \alpha_d$ dual-phase microstructure, exhibiting an improvement in strength and ductility. Although effective, these heat treatments require steps that are carried out outside the AM machine.

In order to minimize this operating constraint, these heat treatments can be performed directly within the AM machine. Because of the layer-by-layer manufacturing of samples, AM allows local control of the microstructure in the bulk of the sample, which is mostly impossible with conventional processes. For instance, Esmaeilzadeh et al. [39] used their machine's laser in defocus mode after sample manufacturing to carry out multiple heat treatments on the same zone in order to initiate the decomposition of the α' phase into $\alpha_d + \beta$. Rietema et al. [40] explored the use of post-build laser scanning to perform layer-by-layer heat treatments on large sample surfaces. Thus far, the use of the primary (printing) laser to directly perform additional heat treatments during manufacturing of Ti-6Al-4V has been reported only for LPBF [41] but not for LDED.

In this work, the aim is to thoroughly understand the impact of in-process laser heat treatments, performed using the primary building laser during LDED of Ti-6Al-4V, on altering the microstructure and improving the mechanical properties (strength/ductility trade-off and toughness) without any post-processing steps. The contribution of each of the microstructural features and internal strains to the overall mechanical response is studied in detail.

2 Materials and methods

2.1 Material

The material investigated in this study is Ti-6Al-4V grade 23 ELI (extra low interstitial) obtained through inert gas atomization by Oerlikon Metco (USA). Powder composition (provided by the supplier) in weight percent (wt%) is the following: Ti – Bal, Al – 6.13, V – 4.13, Fe – 0.15, O – 0.06, C – 0.03, N – 0.01, H – 0.002. Granulometry indicates that the particles' d_{10}, d_{50}, and d_{90} are 53 µm, 70 µm, and 110 µm, respectively. Chemical

analysis using inductively coupled plasma spectroscopy and total organic carbon analysis (FiLAB, France) of the as-built reference sample revealed the following composition (wt%): Ti – Bal, Al – 5.73, V – 4.21, Fe – 0.16, O – 0.094, C – 0.013, N – 0.02, H – 0.0015.

2.2 Additive manufacturing and laser heat treatments

A custom-made miniature laser metal deposition (mini-LMD) machine was used for AM of the studied Ti-6Al-4V; details on the machine design can be found in [42]. It was used to print multiple 60-layered thin wall-shaped samples under an argon atmosphere using a bi-directional single-pass-per-layer printing strategy with the following parameters: laser power = 300 W, printing speed = 10 mm/s, powder flow rate = 2.7 g/min, powder transport gas flow = 0.05 L/min, meltpool enveloping gas flow = 5.0 L/min, and printing head layer increment = 0.24 mm. The mini-LMD's mobile printing head was used to print the samples while keeping the build plate stationary. The continuous-wave fiber laser (wavelength $\lambda = 1080$ nm) is inclined at a $\pm 20°$ angle with respect to the z direction in the $y - z$ plane (coordinate system shown in Figure 1). The powder flow is coaxial with the printing head and the z axis.

The samples were printed on the wide top surface of hot-rolled, annealed and sand-blasted grade 5 Ti-6Al-4V substrates (Comptoir General des Métaux, France) of dimensions 40 $(x) \times 140$ $(y) \times 10$ (z) mm^3. The bottom surface of the substrate was continuously cooled and maintained at $\sim 25°$C during printing with a closed circuit, water-ethylene glycol based, cooling system to facilitate with heat dissipation.

Three different samples were printed using the aforementioned printing strategy. One of the samples, the reference sample, was manufactured without any in-process heat treatment. This sample is designated as the no heat treatment (NHT) sample. The other two samples were subjected to in-process laser heat treatments (LHTs) without powder addition. For one of the two LHT samples, LHT was performed at 100 W and it is henceforth designated as LHT100. For the other sample, LHT was performed at 300 W and it is designated as LHT300.

The following printing and LHT procedure was followed for the LHT100 and LHT300 samples: suppose that n layers have already been deposited and the deposition of the $(n+1)^{\text{th}}$ and $(n+2)^{\text{th}}$ layers is being undertaken as shown in Figure 1:

(i) The $(n+1)^{\text{th}}$ layer is deposited by moving the printing head along y (or $-y$) (Figure 1a).

(ii) Next, for the LHTs, the printing head is then moved back to its position at the start of the printing of the $(n+1)^{\text{th}}$ layer (Figure 1b). Then, the LHTs are performed along the same direction y (or $-y$) and using the same printing head speed as the one used during the printing of the $(n+1)^{\text{th}}$ layer (Figure 1c). Following the LHT, the laser is rotated by 180° (Figure 1d). This entire step takes a total of 52 s. Meanwhile, for the NHT sample, this step is skipped but a laser rotation of 180° together with a dwell time is imposed for a total duration of 52 s (Figure 1d).

(iii) Then, for all samples, the $(n+2)^{\text{th}}$ layer is deposited along the direction opposite to that during the printing of the $(n+1)^{\text{th}}$ layer, i.e., $-y$ (or y) (Figure 1e).

(iv) Step (ii) is then repeated for the LHT and NHT samples but in the opposite direction of laser scanning (Figure 1f-h).

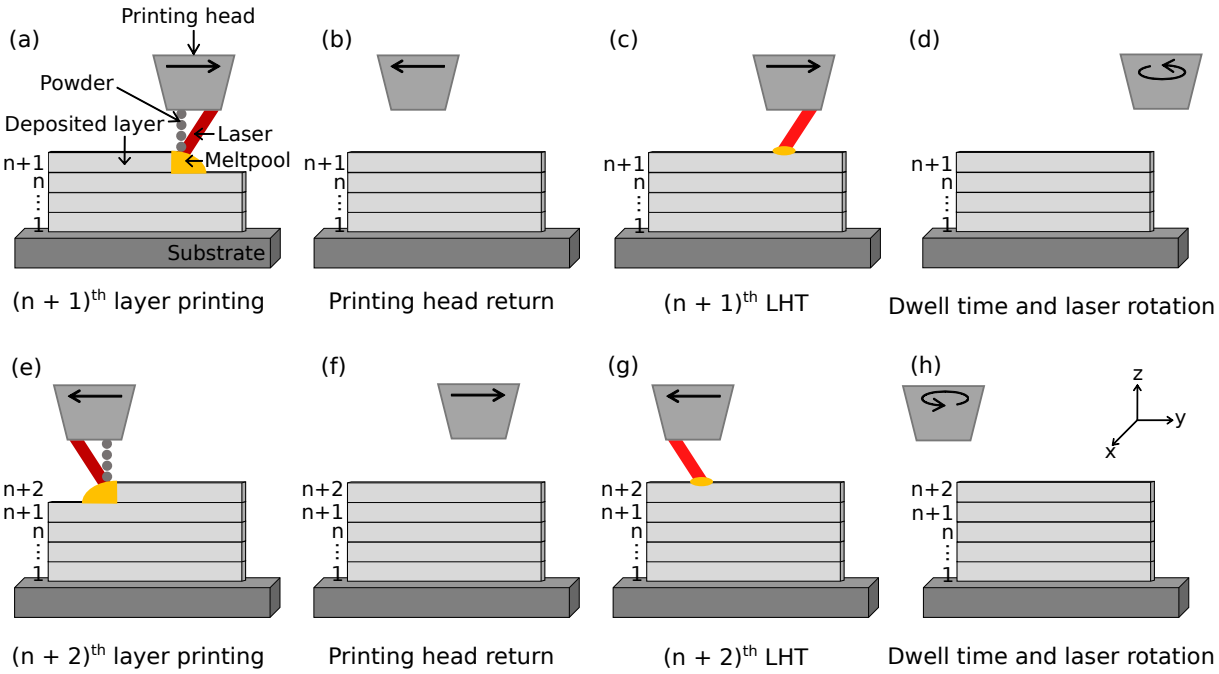

Figure 1: Representation of the sample printing and additional LHT procedure as described in the text.

Steps (i) - (iv) ((a) - (h) in Figure 1) are repeated for the next set of layers until the end of building. From here we can define the building direction (BD) along z and the printing direction (PD) along y. The final dimensions of NHT, LHT100 and LHT300 (Figure 2a-c) samples are 1.81 (x) × 94.2 (y) × 14.8 (z) mm^3, 1.77 (x) × 95.3 (y) × 16.1 (z) mm^3, 1.73 (x) × 93.9 (y) × 15.4 (z) mm^3 respectively. Note that the LHT100 and LHT300 samples exhibit a height higher than the NHT sample, which is counterintuitive because the LHTs should result in remelting and decrease in the height of the sample. However, remelting of the few topmost deposited layers caused by the LHTs results in the working distance between the printing head nozzle and the top of the sample to vary between samples, despite the vertical increments of the focusing head remaining the same for all samples (i.e. 0.24 mm). This change in the working distance causes variations in the layer heights between samples.

2.3 *Ex situ* synchrotron X-ray diffraction

Synchrotron X-ray diffraction (XRD) was performed on the three as-built samples (Figure 2) at room temperature at the ID31 beamline of the European Synchrotron Radiation Facility (Grenoble, France) to study their state after the manufacturing process. A 75 keV monochromatic X-ray beam with a square cross-section and size (1.7 times the full width at half maximum) 230 µm in transmission mode was used to capture diffraction patterns on ±21 mm (175 data points along the y axis) from the center of the manufactured parts, as highlighted by the white rectangles in Figure 2a-c. For each sample, the acquisitions were performed starting from above the top of the sample, i.e., in air, and scanning down until the substrate of the sample is reached. A Pilatus 3X CdTe 2M detector (1475 × 1679 pixels with a pixel size of 172 × 172 µm^2) located at 0.908 m downstream from the samples was used to record the two-dimensional (2D) Debye-Scherrer patterns. Calibration of the detector position, angles, and tilts was performed using cerium dioxide (CeO_2) standard. A representative 2D Debye-Scherrer pattern (averaged over tensile test

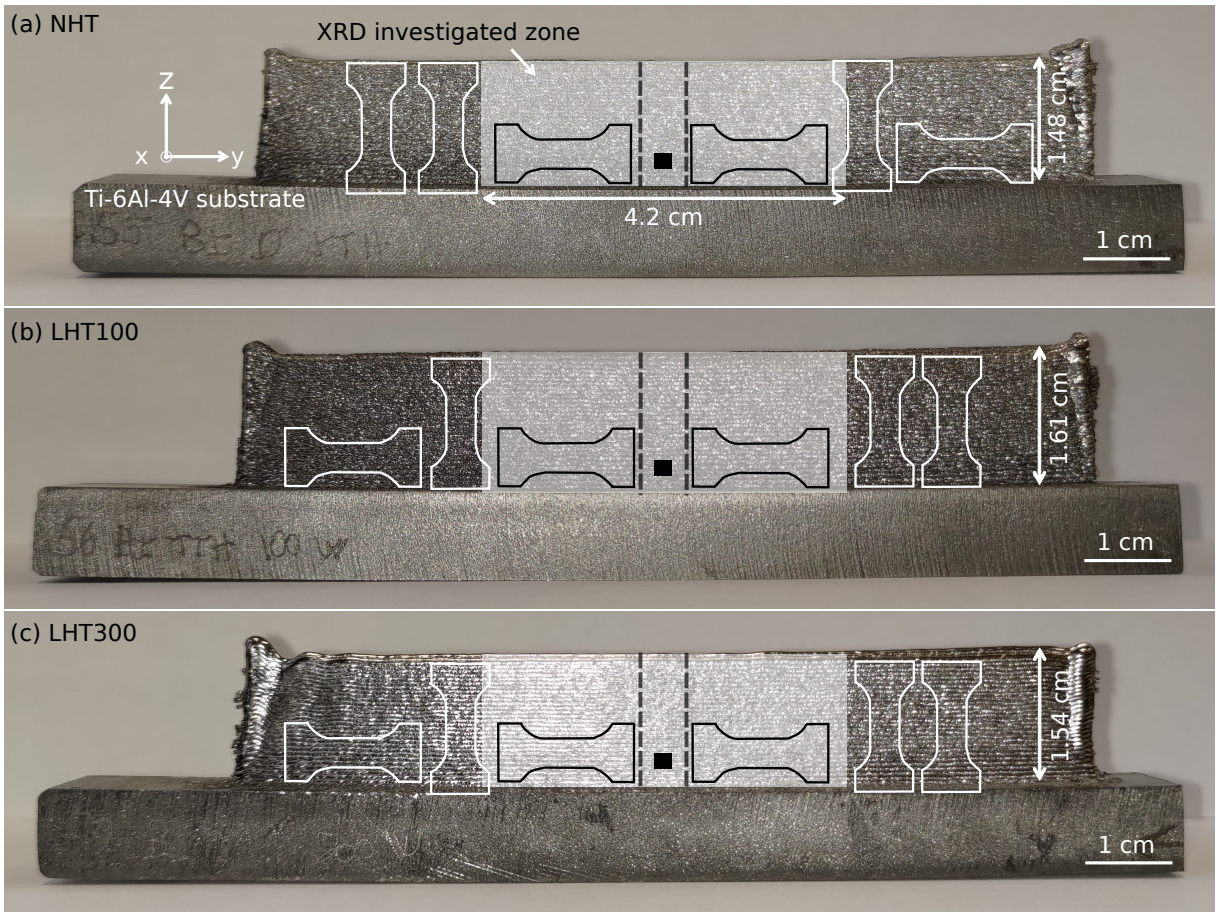

Figure 2: Images of the as-built (a) NHT, (b) LHT100, and (c) LHT300 samples. The white rectangles represent the XRD investigated zones. The dashed lines delimit the specimens extracted for microstructural investigations. The black squares show the zones for scanning and transmission electron microscopy and electron back-scattered diffraction. Dogbone specimens extracted along z (BD) and y (PD) for uniaxial tensile testing are also represented.

specimen gauge area) for each sample is shown in Figure 3a-c for NHT, LHT100, and LHT300, respectively.

In order to obtain the hcp and bcc phase content via Rietveld refinement, the 2D Debye-Scherrer patterns from the as-built samples were azimuthally integrated over a 360° angular range using PyFAI (Python library) [43] to obtain the azimuthally integrated diffraction (intensity I versus 2θ) line profiles. The azimuthal integration also considered the intermodular distortions of the detector. A representative line profile from an as-built sample is shown in Figure 3d. Then, Rietveld refinement was performed on the azimuthally integrated I vs 2θ diffraction line profiles [44] via the FullProf suite [45] with a pseudo-Voigt function in sequential mode. The crystal structures of hcp (space group = P63/mmc) and bcc (space group = Im-3m) titanium phases considered were obtained from the Crystallographic Open Database (CIF files 9008517, 9012924 [46]). The Rietveld fit of the line profile represented in Figure 3d is also shown in the same figure. The "goodness of fit" and the residual differences between observed and calculated intensities [47, 48] were used to evaluate the quality of the fits.

The azimuthally integrated diffraction line profiles were also used to obtain the Williamson-Hall ($\Delta\theta \cos\theta$ vs. $\sin\theta$) plots using all the peaks in order to study the intragranular strain

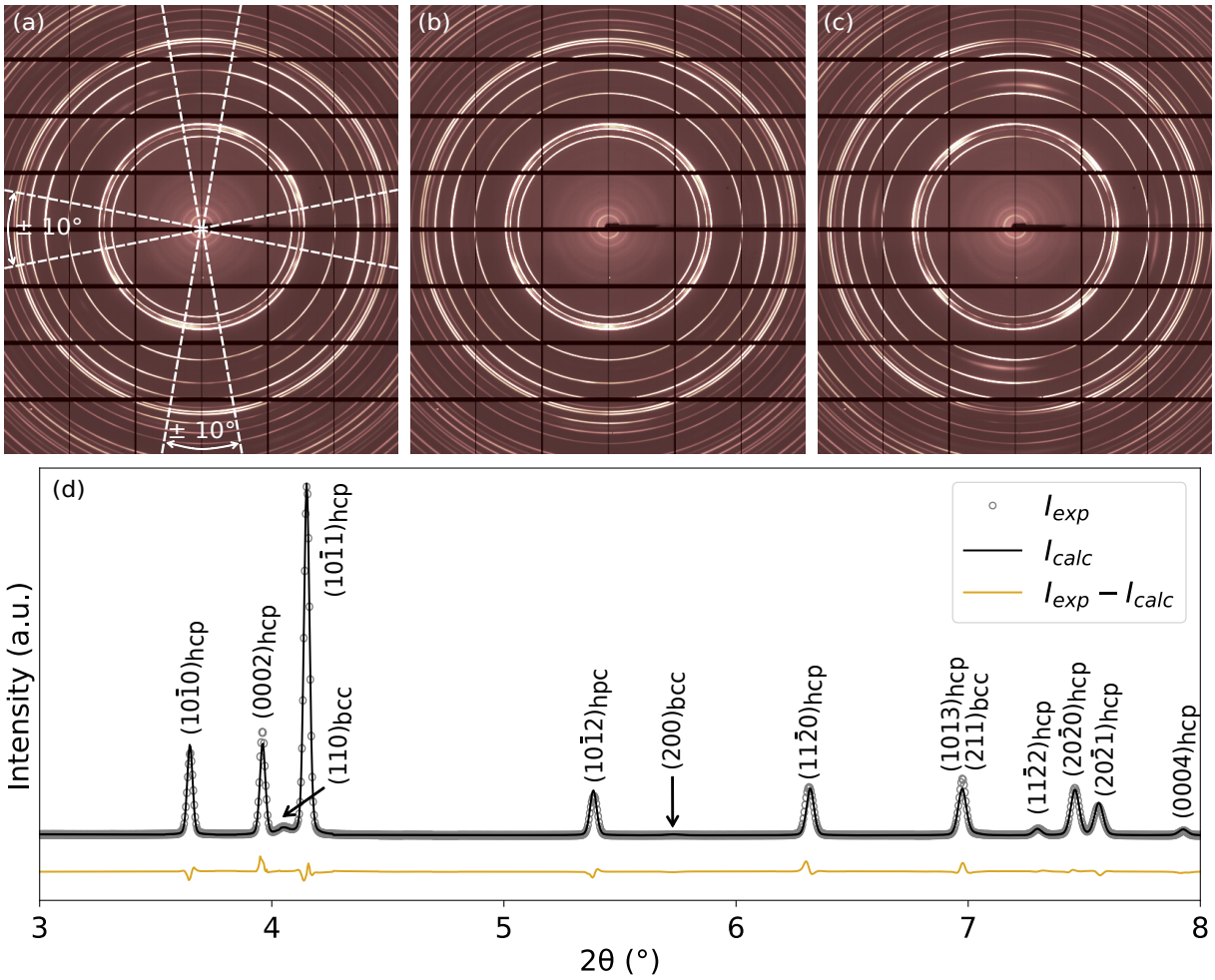

Figure 3: Representative 2D Debye-Scherrer patterns of (a) NHT, (b) LHT100 and (c) LHT300 as-built Ti-6Al-4V samples. (d) A representative XRD line profile (I vs. 2θ) obtained after integrating over the entire azimuthal angle and used for Rietveld refinement. The experimental intensity, the one calculated from the Rietveld fit and their difference are shown in (d). The black arrows highlight the faint bcc diffraction peaks. The $\pm 10°$ portions of the 2D Debye-Scherrer rings used to obtain the lattice parameters along BD and PD, the about the vertical and horizontal directions are also represented by white dashed lines in (a).

and crystallite size distributions in samples; $\Delta\theta$ is the full width at half maximum.

In order to obtain the lattice parameters along BD and PD, the $\pm 10°$ portions of the 2D Debye Scherrer rings about the vertical and horizontal directions (Figure 3a), respectively, were separately integrated. Lattice parameters c and a of the hcp phase were obtained from the 0002 and 11$\bar{2}$0 peaks, respectively, based on [49].

2.4 Scanning and transmission electron microscopy

To investigate the microstructural features, samples were cut across the cross-section (x-z plane), and specimens of size (represented by the dashed black lines in Figure 2): wall thickness (x) × 5 (y) × wall height (z) mm^3 extracted from the middle of the as-built parts using a cutting machine (Struers). They were cold-mounted in an epoxy resin, mechanically polished with silicon carbide (SiC) abrasive sandpaper to P2400, and diamond paste polished down to 1 µm. Finishing step involved a 27-hour vibrometer

polishing using a MasterMet solution (Bühler) combined with 10 mL of H_2O_2. A 10 nm layer of carbon was deposited to ensure a good conductivity during scanning electron microscopy (SEM) observations.

Electron back-scattered diffraction (EBSD) imaging of the cross-sections was performed in a FEI quanta 600 FEG SEM equipped with a symmetry detector (Oxford Instruments). EBSD maps of the cross-section were acquired at 15 keV with a spot size of 6.5 and a step size of 0.2 μm with an acquisition time of 5.32 ms and a 10% overlap between each 300 $\times$ 400 μm^2 field. In order to map the entire cross-section of each sample, 7 acquisitions were needed. Each cross-sectional map has an area of 1920 $\times$ 400 μm^2. For each sample, the EBSD acquisition time was 60 hours. EBSD analysis was performed using AZtec 6.0 SP1 software considering the hcp and bcc phases of titanium. The indexation rate prior to image processing was greater than 70% for all the samples. Post-processing was carried out using AZtec Crystal 3.0 software.

Next, energy-dispersive X-ray spectroscopy (EDS) investigations were achieved at Synergie 4 (France) using a flatquad detector (Bruker) in a JEOL IT 500 HR with an acquisition time of 5 hours at 6 keV with $\sim$ 130,000 counts per second.

Following this, a mixture of 10 mL KOH, 5 mL H_2O_2, and 20 mL H_2O was used during 30 s to etch the polished specimens. Back-scattered electron (BSE) imaging was performed using the FEI quanta 600 FEG SEM equipped with a BSE detector (Thermo Fisher). For each cross-section of an etched specimen, 12 regions each of 227 $\times$ 331 μm^2 size were mapped at 0.2 μm resolution. Then, using the Fiji (ImageJ) [50] software, all images were converted to 8-bit (to perform thresholding) and the gray histogram of each acquisition was centered to 128. The 12 treated images from each specimen were then stitched together using Fiji with the procedure described in [51].

Finally, focused ion beam was used to extract thin-film lamellae of approximately 100 nm thick inside a FEI Helios Nanolab 660 dual-beam SEM, which were investigated using a Titan G2 TEM microscope featuring a Cs probe corrector, STEM detectors, and a SuperX detector with EDS capabilities to investigate the chemical heterogeneities and identify the retained β phase.

2.5 Uniaxial tensile testing

For the tensile tests, dogbone specimens were machined from the manufactured parts vertically along z (BD) and horizontally along y (PD), and polished using grit SiC sandpaper up to P2400 to remove surface roughness. All vertical and horizontal dogbones have been extracted at the same height (z axis) with respect to the substrate. For NHT and LHT300 samples, one side of the three dogbones was extracted in the Ti-6Al-4V substrate along z. The gauge region of each sample had dimensions of 0.98 (x) $\times$ 2.25 (y) $\times$ 4.5 (z) mm^3 to respect a length-to-width ratio of 2.

To ensure representativeness of the results, three specimens per direction were extracted from each sample as shown in Figure 2 and tested using an in-house built uniaxial tensile testing machine with a strain rate of 2 μm/s and a 5 kN force cell. A Sill Optics correctal camera and marker tracking were used to measure the deformation during tensile testing. Following failure, secondary electron (SE) imaging was performed with the FEI Quanta 600 FEG SEM to image the fracture surface of the specimens.

3 Results

Three samples were built using the printing and LHT strategy described in Section 2.2: NHT (without any heat treatment), LHT100 and LHT300 (with in-process laser heat treatment at 100 W and 300 W, respectively, after each layer deposited). *Ex situ* synchrotron XRD was performed on each as-built sample prior to extracting them from the substrate. Then, from the center of the samples, slivers were machined out for microstructure analysis (see Section 2.4 for preparation) in the SEM. Finally, dogbone shaped samples were extracted for uniaxial tensile testing (see section 2.5 for preparation). The results of these tensile tests are first presented.

3.1 Effect of LHT on the mechanical response

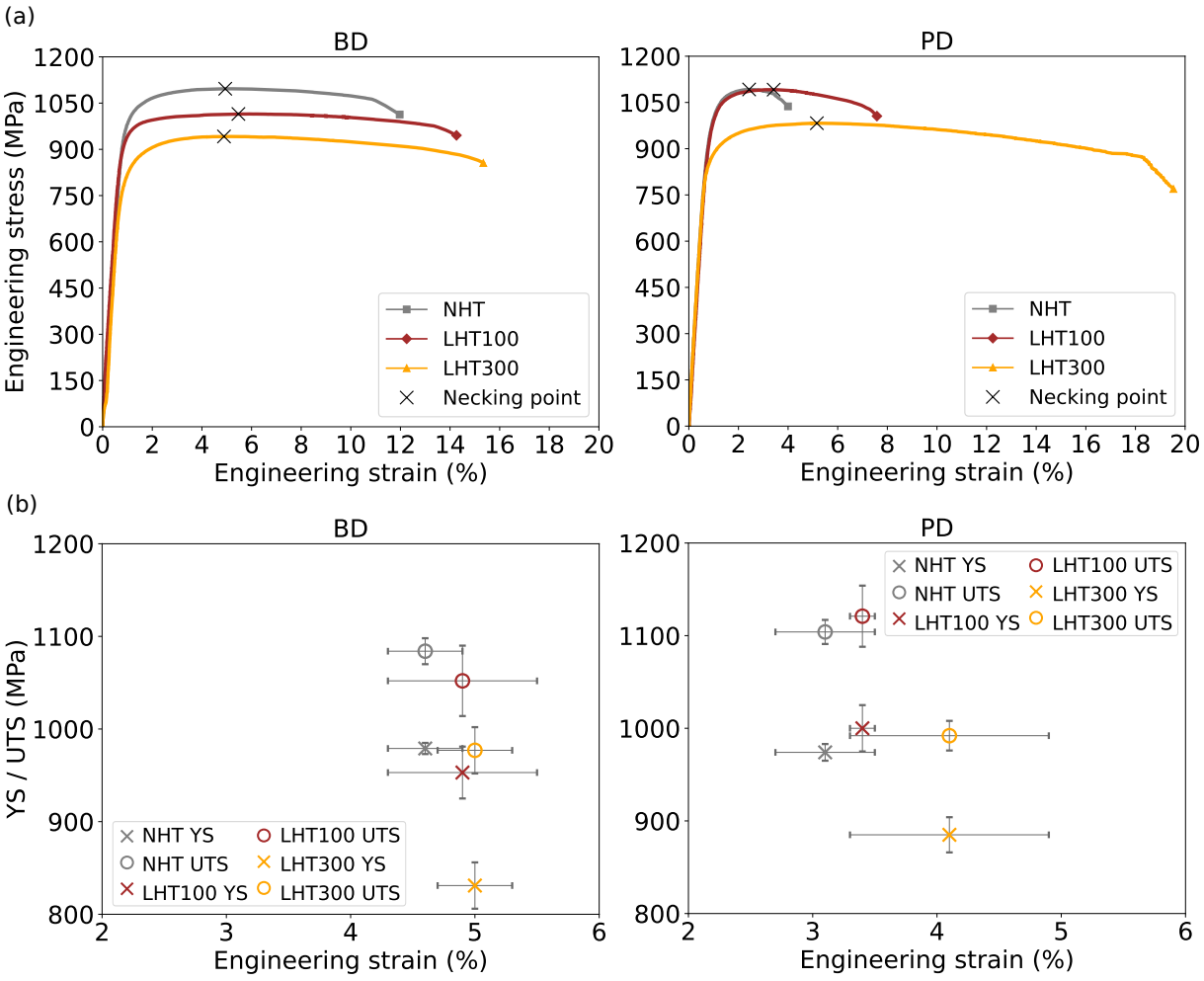

Figure 4: (a) Engineering stress vs. engineering strain curves from representative tensile specimen extracted along BD (z) and PD (y). (b) Mean and standard deviation of the yield strength (YS) and ultimate tensile strength (UTS) as a function of maximum elongation prior to necking for NHT, LHT100, and LHT300 along the BD and PD.

Two sets of three dogbone shaped specimens were extracted from each NHT, LHT100, and LHT300; one set was along BD (z) and the second set was along PD (y). Figure 4 illustrates the representative engineering stress-strain curves and the yield and ultimate tensile strengths as a function of maximum elongation prior to necking from the two sets

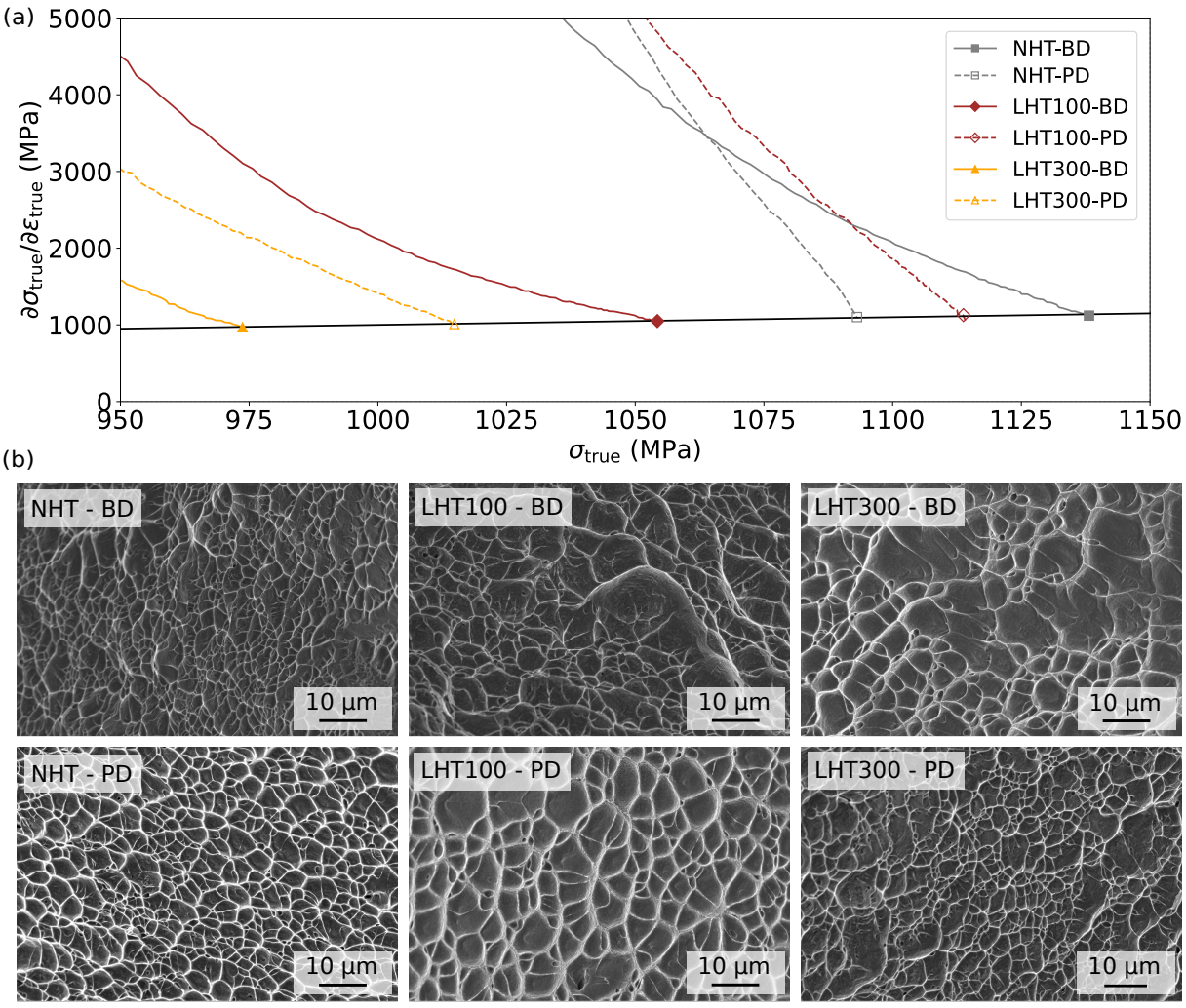

Figure 5: (a) Tangent modulus of the true stress-strain curves as a function of true stress for the NHT, LHT100, and LHT300 samples. The solid black line represents the Considère criterion. (b) Fractography along z (BD) and y (PD) for NHT, LHT100, and LHT300.

for these samples. As shown in Figure 5a and Figure S1, all specimens tested satisfied the Considère criterion and failed in the gauge area. Furthermore, fractography analysis presented in Figure 5b reveals typical ductile fracture features characterized by a homogeneous distribution of dimples on the fracture surface; no abnormal features such as pores or cracks were detected on the fracture surface of any specimen. The results shown in Figure 5 indicate that the full deformation potential of the material was reached prior to failure. Based on this understanding, a deeper analysis of the results can be undertaken. Table 1 shows the statistics of the Young's modulus and modulus of toughness for all the specimens.

For each sample, the mean values of the Young's moduli are similar between PD and BD indicating that samples are at least transversely isotropic in the $y-z$ plane from a macroscale elasticity standpoint. Between the different samples, the Young's moduli of LHT100 and LHT300 are similar and slightly lower than NHT along BD. Whereas along PD the Young's moduli of NHT, LHT100, and LHT300 are similar. However, the standard deviation of the Young's moduli is such that there is practically no difference between and within each sample. Therefore, the additional LHTs do not impact the Young's modulus.

The representative tensile test curves, presented in Figure 4a, exhibit a significant

Table 1: Mean and standard deviation of Young's modulus (E) and modulus of toughness of NHT, LHT100, and LHT300. Percentage difference of the mean values of LHT100 and LHT300 with respect to NHT.

		NHT	LHT100	% diff. with NHT	LHT300	% diff. with NHT
E (GPa)	BD	130 ± 4	121 ± 4	-6.9	125 ± 7	-3.8
	PD	126 ± 6	128 ± 2	1.6	126 ± 0.6	0
Toughness (MPa)	BD	107 ± 12	116 ± 22	8.4	150 ± 13	40.2
	PD	54 ± 22	72 ± 9.4	33.3	96 ± 60	77.8

difference in the yield strength (at 0.2% plastic strain), ultimate tensile strength, and maximum elongation prior to necking between the three samples along both directions. Along BD, NHT, LHT100, and LHT300 exhibit the highest, intermediate and lowest, respectively, yield and ultimate tensile strengths. This trend is reversed for the maximum elongation prior to necking. Meanwhile, along PD, LHT100, NHT, and LHT300 respectively exhibit the highest, intermediate and lowest yield and ultimate tensile strengths. However, interestingly, the trend in the maximum elongation prior to necking is the same as that along BD. Therefore, along PD, LHT100 demonstrates a better strength/ductility trade-off than NHT. For both BD and PD, NHT, LHT100, and LHT300 demonstrate the lowest, intermediate and highest toughness. However, along PD, the standard deviation in toughness of LHT300 is very high.

Collecting these results, it is clear that LHT100 results in better strength than LHT300 but the latter results in better ductility and toughness. In comparison to NHT, LHT100 also results in an overall improvement in the strength-ductility trade-off and toughness. Meanwhile, LHT300 results in a reduction in strength but a significant increase in ductility and toughness in comparison to NHT.

These differences in the mechanical response must arise from the combined effect of microstructural features and internal (intergranular and intragranular) strains. To understand these contributions, a combination of synchrotron XRD, SEM and TEM analyses was conducted on the as-built samples.

3.2 Quantifying constituent phase fractions

3.2.1 Rietveld refinement to separate hcp and bcc fractions

Prior to the extraction of dogbones, non-destructive synchrotron XRD measurements had been performed on each sample with the aim to quantify phase fractions and compute microstrain distributions in the as-built state with the substrate still attached.

The only discernible peaks on the representative I vs 2θ diffraction line profile presented in Figure 3d are those from the hcp and bcc phases. The hcp phase could include a combination of α', α_d, and α_m. However, they cannot be distinguished from XRD measurements, indicating that they have similar lattice parameters, which is consistent with the existing literature [52, 53]. Meanwhile, the bcc phase is retained β, the only known bcc phase to occur in Ti-6Al-4V at room temperature. Therefore, synchrotron XRD measurements are used only to separate the retained β phase and the collective set of hcp phases.

The diffraction line profile reveals one set of high-intensity peaks of the hcp phase and a low-intensity (110) bcc peak located between the (0002) and $(10\bar{1}1)$ hcp peaks. The

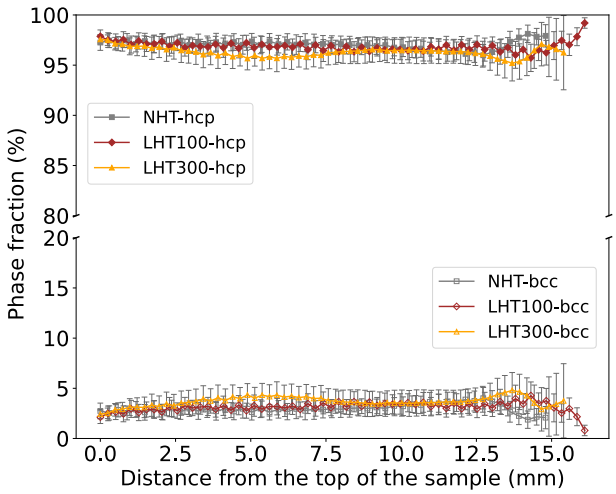

Figure 6: Hcp and bcc average phase fraction distribution as a function of distance from the top of the as-built samples along $-z$ for NHT, LHT100, and LHT300.

significant intensity difference between the hcp and bcc peaks implies a low amount of retained β. Rietveld refinement is performed to quantify the phase fractions and their distribution is plotted in Figure 6. All three samples show a similar distribution of the phases all along the height for the three samples; the mean (and standard deviation) values for NHT, LHT100, and LHT300 for the hcp phase are 97% ($\pm$ 1.0%), 96.9% ($\pm$ 1.1%) and 96.3% ($\pm$ 1.5%) respectively, and for the bcc phase are 3.0% ($\pm$ 1.0%), 3.1% ($\pm$ 1.0%) and 3.7% ($\pm$ 1.5%), respectively. Phase fraction fluctuations within each plot are influenced by the surface roughness of the samples and the low intensity of the most intense β peak, i.e. 110, which appears between two very close 0002 and $10\bar{1}1$ hcp peaks. Note that the standard deviation for each sample falls into the minimum error of the Rietveld refinement. Nevertheless, the differences in the mean values and standard deviations (i.e., variations within a sample) of each phase between the samples are small. Therefore, it can be concluded that additional LHT does not result in any significant differences in the hcp and bcc phase fractions between the samples.

In all samples, the amount of retained β is between 3.0% and 3.7%. Such small fractions cannot solely explain the significant differences in the mechanical response. More significant contributions are likely coming from other microstructural features.

3.2.2 Identifying hcp phase constituents: microstructural investigations

SEM analysis was performed on the cross-sections (x-z plane) of the three as-built samples to identify the hcp phase constituents. As mentioned at the beginning of section 3, the samples have different heights and to facilitate comparison, SEM analysis is performed in the height range between 2.35 - 2.75 mm above the substrate (represented by the black rectangles in Figure 2) and across the thickness of all the samples; note that the analyses were restricted to this zone because performing EBSD at a resolution of 0.2 μm, which was deemed to be the minimum necessary to resolve α'/α_d phases, took a significant amount of time (60 hours) per sample. This height range also corresponds to a zone sufficiently away from the substrate such that the chemical composition of the material is not affected by proximity to the substrate. In addition, this region is at a height much lower than the sample height, which allows for studying the impact of multiple SSTCs on the sample.

Figure 7 shows the EBSD (IPF z coloring) and higher magnification views of EBSD along with BSE maps of the studied portion of the cross-section for the three samples.

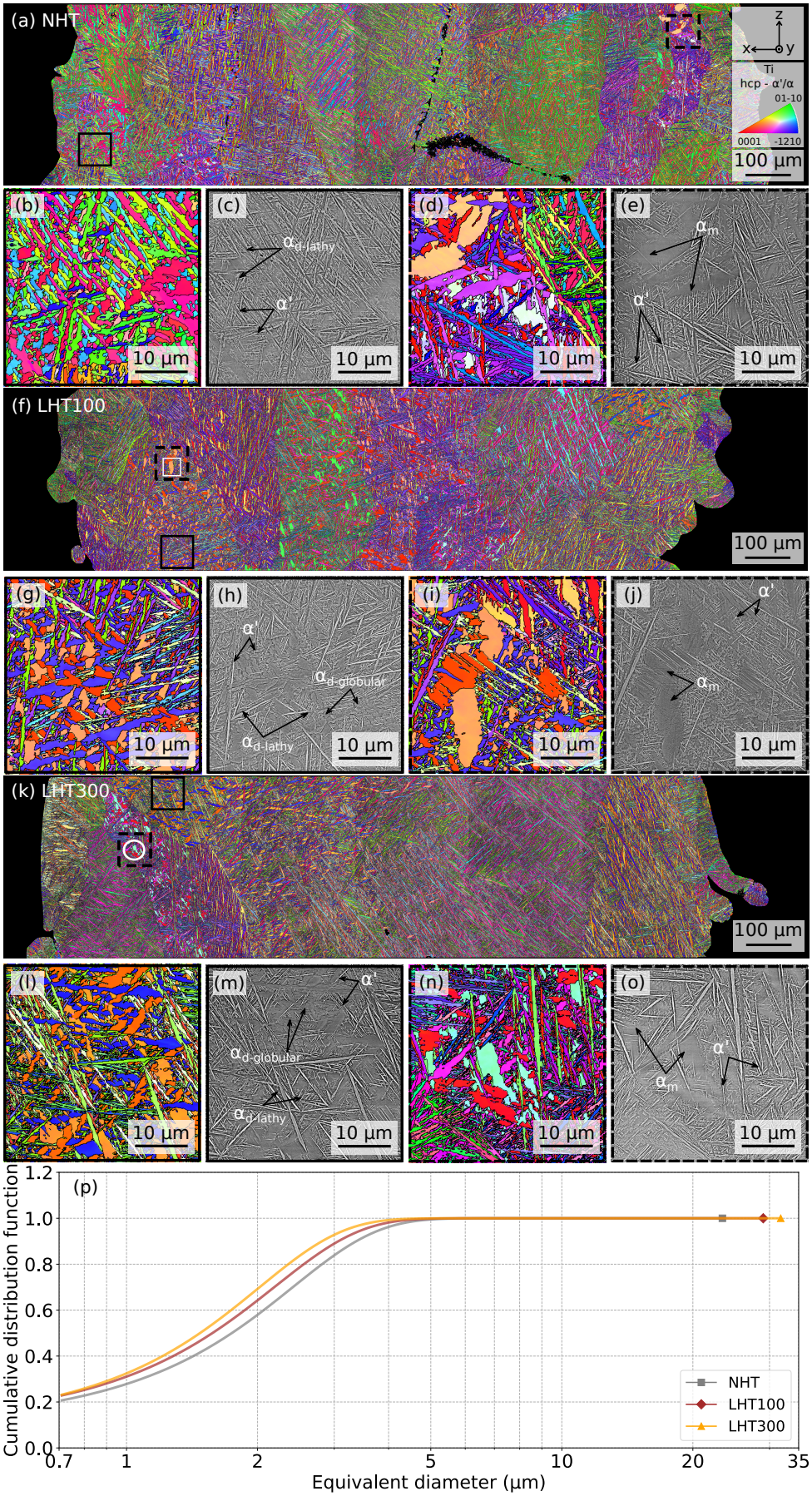
(a) NHT
Z
X
Y
Ti
hcp - α'/α
01-10
0001
-1210
100 μm
(b)
10 μm
(c)
$\alpha_{d\text{-}lathy}$
α'
10 μm
(d)
10 μm
(e)
α_m
α'
10 μm
(f) LHT100
100 μm
(g)
10 μm
(h)
α'
$\alpha_{d\text{-}globular}$
$\alpha_{d\text{-}lathy}$
10 μm
(i)
10 μm
(j)
α'
α_m
10 μm
(k) LHT300
100 μm
(l)
10 μm
(m)
α'
$\alpha_{d\text{-}globular}$
$\alpha_{d\text{-}lathy}$
10 μm
(n)
10 μm
(o)
α'
α_m
10 μm
(p)
Cumulative distribution function
0.0
0.2
0.4
0.6
0.8
1.0
1.2
0.7
1
2
5
10
20
35
Equivalent diameter (μm)
NHT
LHT100
LHT300

Figure 7: (a, f, and k) EBSD maps with 0.2 μm from the cross-section of the NHT, LHT100 and LHT300 samples. (b-e), (g-j) and (l-o) EBSD and BSE high magnification views (plain and dashed squares) of different zones in the investigated cross-section. The plain white square in (f) represents thin lamellae extraction zones from an α_m grain. The white circle in (k) represents the investigated zone for EDS analysis shown in Supplementary material Figure S4. Color code in EBSD images is according to IPF z whose key is shown in (a). The coordinate system is also presented in (a). Both apply to all samples. (p) Grain size distribution for NHT, LHT100, and LHT300.

The β phase, whose volume fraction in each sample is less than 3.7% (Section 3.2), could not be identified in any map (see Supplementary material Figure S2), indicating that the grain size of retained β is smaller than the EBSD resolution (0.2 μm); this result is confirmed by TEM analysis presented in the Supplementary material Figure S3. The EBSD maps allow identifying grains and analysing them individually. Meanwhile, the zoomed-in BSE images in Figure 7 allow a clear identification of the different hcp phases through the contrast within each image of a specimen. These differences arise due to the combined contribution of the segregated heavy (vanadium and iron) and light (aluminum and oxygen) elements, which, respectively, create a bright and dark contrast.

To test whether the different phases can be isolated based on their chemical composition, an EDS analysis was carried out in the SEM on a region in LHT300 that is representative of the three hcp phases in each sample. However, the results were inconclusive due to the difficulty of separating the hcp phases using elemental segregation of α_d and β stabilizers. The images showed a homogeneous distribution of Al and V in the region tested (see Supplementary material Figure S4); therefore, the EDS imaging in SEM was not used further.

Therefore, the focus in the microstructural analysis is kept on the EBSD and BSE images. Four discernible populations of hcp grains can be identified: acicular grains with the highest intensity in BSE images, lath-shaped grains with medium intensity, globular grains with medium intensity and irregularly-shaped coarser grains with the lowest intensity in the bulk.

The acicular-shaped grains with the highest intensity belong to the martensitic α' phase. The BSE image reveals different sizes of these grains that are not visible in the EBSD image. According to Yang et al. [54], different sized needles of α' form during the initial stages of SSTC, with the largest forming during the first cooling down after deposition.

The lathy and globular shaped grains are typically from the α_d phase that arises partly during the cooling down from above the β transus (some portion of the material may have lower cooling rates than those that yield the α' phase), and from the breakdown of α' phase into α_d and β due to the subsequent SSTC. Finally, the irregularly-shaped coarser grains are identified as the α_m phase. The α' and α_d phases are rather homogeneously distributed across the microstructure, whereas clusters of α_m, which are lower in proportion, are heterogeneously distributed.

Based on the morphology of α_m grains from EBSD maps and the brightest intensity of α' in the BSE images, these phases are manually segmented to obtain comparable measures of their area fractions. These measures are then used to deduce the fraction of the combined globular and lathy α_d phase. In what follows, the procedure to isolate each hcp phase is described:

- Due to the irregular shape of α_m grains, there is no established procedure to segment them from images. Furthermore, due to a relatively large area studied, manual segmentation was deemed unfeasible. Instead, the following two-step selection approach that could be implemented in the EBSD software (Aztec) was devised: (i) Select grains that have an area greater than or equal to 40 μm^2 in the entire microstructure. (ii) Deselect grains that have length-to-width ratio (of an adjusted ellipse) greater than 5. The first criterion avoids selecting globular α_d, which are smaller in size than the α_m grains, and the two criteria together avoid selecting acicular α' and lathy α_d. The EBSD maps for the distributions of these phases are shown in Supplementary Figure S5. Due to a low amount of these phases in the studied EBSD cross-section, another cross-section (at height 1.95 - 2.35 mm along BD) was also studied to improve statistics (see Supplementary Figure S6 for the EBSD cross-section and Supplementary Figure S7 for the phase distribution). Note that the numbers used in the selection criteria are specific to our samples and may differ for samples fabricated using different printing parameters. Furthermore, while the accuracy of the extracted data may not be perfect, nevertheless they highlight the correct trend between samples; computing the error involved would require manual segmentation of each α_m grain, which is also error-prone (based on the investigator) and impractical as mentioned earlier.

- Next, the fraction of the α' phase was obtained from BSE images (Figure 7). For each cross-sectional image, a manual grayscale thresholding was performed to select only the acicular phases, which appear as the brightest (highest intensity) features.

- Combining the contributions of α_m, α', and β (from Section 2.3), the fraction of combined lathy and globular α_d can be deduced.

- Assuming that the area fractions, measured over a large area, are similar to the volume fractions, the adjusted volume fractions of all the identified hcp phases and the bcc β phase for each sample are computed.

Figure 8 shows the proportions of each phase computed using the aforementioned criteria. Between the hcp phases of each sample, α_d has the highest phase fraction followed by α' and α_m. Across samples, the α' fraction is the highest in NHT and lowest in LHT300, α_m is the highest in LHT100 and lowest in LHT300, and α_d is the highest in LHT300 and lowest in NHT.

The dominant hcp phase is α_d followed by α'. The ratio of α' to α_m is 8.8, 4, and 10.1 in NHT, LHT100, and LHT300, respectively. Meanwhile, the ratio of α' to α_m is 32, 9.6, and 40.7 in the same order.

For an LDED process with the highest cooling rates that can reach up to 10^5 K/s [55, 56], the proportion of α' martensite appears to be uncharacteristically low. However, note that the microstructure investigations have been conducted on a layer that has been subjected to multiple SSTCs with decreasing temperature amplitudes and heating/cooling rates that should result in the decomposition of α' into α_d and β. The ratio of α'/α_d is expected to increase with increasing height (along the BD) as has been consistently shown in the literature [17, 57].

3.3 Lattice parameter evolution and Williamson-Hall plots

The synchrotron XRD data used to obtain the hcp and bcc phase fractions in Section 3.2.1 is also used to study the lattice parameter distribution and peak widths through

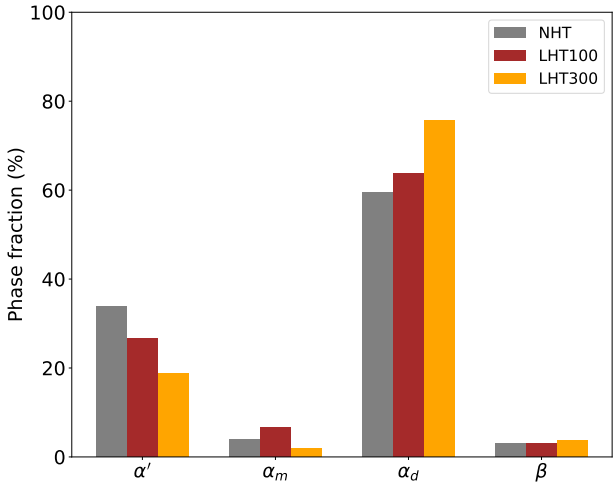

Figure 8: Percentage phase fractions of bcc and adjusted hcp phases obtained from Rietveld refinement in Section 3.2.1 and SEM analysis in Section 3.2.2.

the Williamson-Hall plot [58] in the as-built samples as described in Section 2.3.

For the lattice parameters, instead of integrating the Debye-Scherrer rings over the entire azimuthal range, they are caked (divided) into angular portions of 10° each and two portions ±10° around BD and around PD are analysed (Figure 3a). Line plots of lattice parameters averaged per layer as a function of the distance from top of the sample are shown in Figure 9; a Butterworth low-pass filter was applied to the data to improve visualization. The plots reveal very small differences in magnitudes and evolution between samples in either direction. This similarity indicates that LHTs do not result in any significant differences in lattice parameters. The mean and standard deviation of a and c for each sample along both BD and PD are shown in Table 2. Their near perfect match implies that there are no major chemical and/or mechanical differences between the different as-built samples. Furthermore, it can be deduced that residual intergranular strain distributions, which must relax equally in all samples after dogbone extraction due to the macroscopic elastic (transverse) isotropy of the material, do not play any significant role in the variation of the mechanical response between NHT, LHT100 and LHT300.

Figure 10 shows the Williamson-Hall [58] plot obtained from I vs. 2θ plots after azimuthally integrating the entire Debye-Scherrer rings for each sample. It provides an estimate for the crystallite size averaged over the domain and intragranular lattice strain distributions arising from dislocation populations (both geometrically necessary and statistical i.e., Nye's dislocation density tensor is non-zero and zero, respectively). Apart from one point for the LHT300 sample with a larger spread, there is a near perfect match between the samples; the large spread in LHT300 is occurring due to very noisy data that results in a poor fit. Nevertheless, further analysis of this plot is not necessary because this result indicates that the probed volume-averaged intragranular strain distributions, which arise from dislocations, and the crystallite size distributions are nearly the same for all samples. These results are also supported by the geometrically necessary dislocation density distributions discussed in Section 3.4.

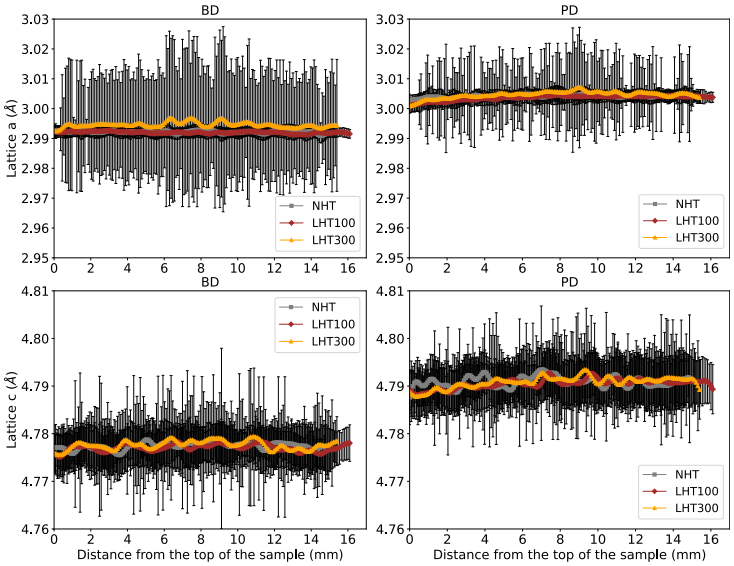

Figure 9: Line plots of a and c lattice parameter of the hcp phase, averaged per layer as a function of distance from top of the sample for (a) BD (z axis) and (b) PD (y axis) for NHT, LHT100, and LHT300 samples. LHT300 exhibits the widest spread in standard deviation.

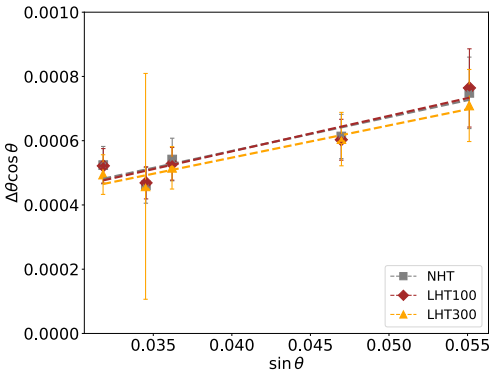

Figure 10: Williamson-Hall plots with the standard deviation, from the diffraction line profiles extracted from the full 2D Debye-Scherrer pattern shown in Figure 2a-c.

Table 2: a and c lattice parameters for both BD and PD.

	NHT (stdev)	LHT100 (stdev)	LHT300 (stdev)
a_{PD} (Å)	3.004 (±0.002)	3.004 (±0.0023)	3.005 (±0.0103)
a_{BD} (Å)	2.992 (±0.0018)	2.992 (±0.0016)	2.995 (±0.019)
c_{PD} (Å)	4.791 (±0.0052)	4.790 (±0.0048)	4.791 (±0.0080)
c_{BD} (Å)	4.777 (±0.0044)	4.777 (±0.0038)	4.778 (±0.0082)

Table 3: Grain sizes and GND density for NHT, LHT100 and LHT300.

	NHT (stdev)	LHT100 (stdev)	LHT300 (stdev)
Grain size (μm)	1.75 (±1.27)	1.58 (±1.16)	1.48 (±1.04)
GND $\times 10^{14}$ (m^{-2})	3.1 (±1.5)	3.4 (±1.7)	3.5 (±1.8)

3.4 Grain size and geometrically necessary dislocation density distributions

Figure 7p shows the cumulative distribution function plot for the grain sizes obtained from the EBSD maps of Figure 7a, f and k for the three samples. Table 3 shows the mean and standard deviations of the grain sizes. The grain sizes are highest in NHT and smallest in LHT300. Although the differences between samples may appear small, they could result in significant differences in the strength of the material. To obtain a measure of their potential contribution, the Hall-Petch relationship proposed in [59] for primary α grains whose tendency is most representative of the response observed in this work is used: $\sigma_{YS}(\text{MPa}) = 230d^{-0.5} + 737$, where d is the grain size in (μm). Of particular importance is the term $230d^{-0.5}$. Using the mean grain sizes reported in Table 2, this term is 174 MPa, 183 MPa, and 189 MPa for NHT, LHT100 and LHT300, respectively. This result implies that, solely on the basis of grain size, LHT300 should result in the highest yield strength followed by LHT100 and NHT. However, the trend observed in Figure 4 is the opposite. Furthermore, the difference between the highest and lowest magnitudes of the aforementioned term is only 16 MPa, which is an order of magnitude lower than the difference in yield strength between NHT and LHT300. Therefore, small differences in grain sizes are expected to play a minor (if not negligible) role in determining the mechanical response.

Another difference in mechanical response could arise from variations in the strengthening effect caused by different dislocation densities. In Section 3.3, the Williamson-Hall plot from the three samples matched nearly perfectly, indicating that the contribution of intragranular strain distributions arising from all dislocation populations to the mechanical response is nearly the same. However, sub-populations of dislocations, specifically geometrically necessary and statistical dislocations, could vary and result in different contributions.

In order to study the role of geometrically necessary dislocations, their density is evaluated from the EBSD results shown in Figure 7; note that this density magnitude is subject to the EBSD resolution used and yet it will give an indication on the contribution of this population. Figure 11 shows the geometrically necessary dislocation density maps of the three samples along with their distribution functions.

Overall, there are minor (and possibly negligible) differences in the magnitudes and distributions of these densities between the samples. The mean and standard deviations of the densities over the studied domains are shown in Table 3. They demonstrate a near-perfect match between the samples. Since the strength of the material is proportional to the square root of the dislocation density, the contribution of geometrically necessary dislocation density to the difference in mechanical response between samples is negligible. Combined with the negligible difference in the Williamson-Hall plots, it can be concluded that the geometrically necessary and statistical populations of dislocations are similar between the samples.

However, there are significant differences in the geometrically necessary dislocation densities between α_m and the remaining two hcp phases ($\alpha' + \alpha_d$) in all samples; α_m consistently shows at least an order of magnitude lower densities. However, due to the relatively low fraction of α_m in all samples, and the understanding that this phase has an intermediate strength between α' and α_d [32], this difference in geometrically necessary dislocation densities should not play a significant role in determining the mechanical response; however, a deeper analysis (possibly involving nanoindentation studies) is required to corroborate this statement, which is beyond the scope of this work.

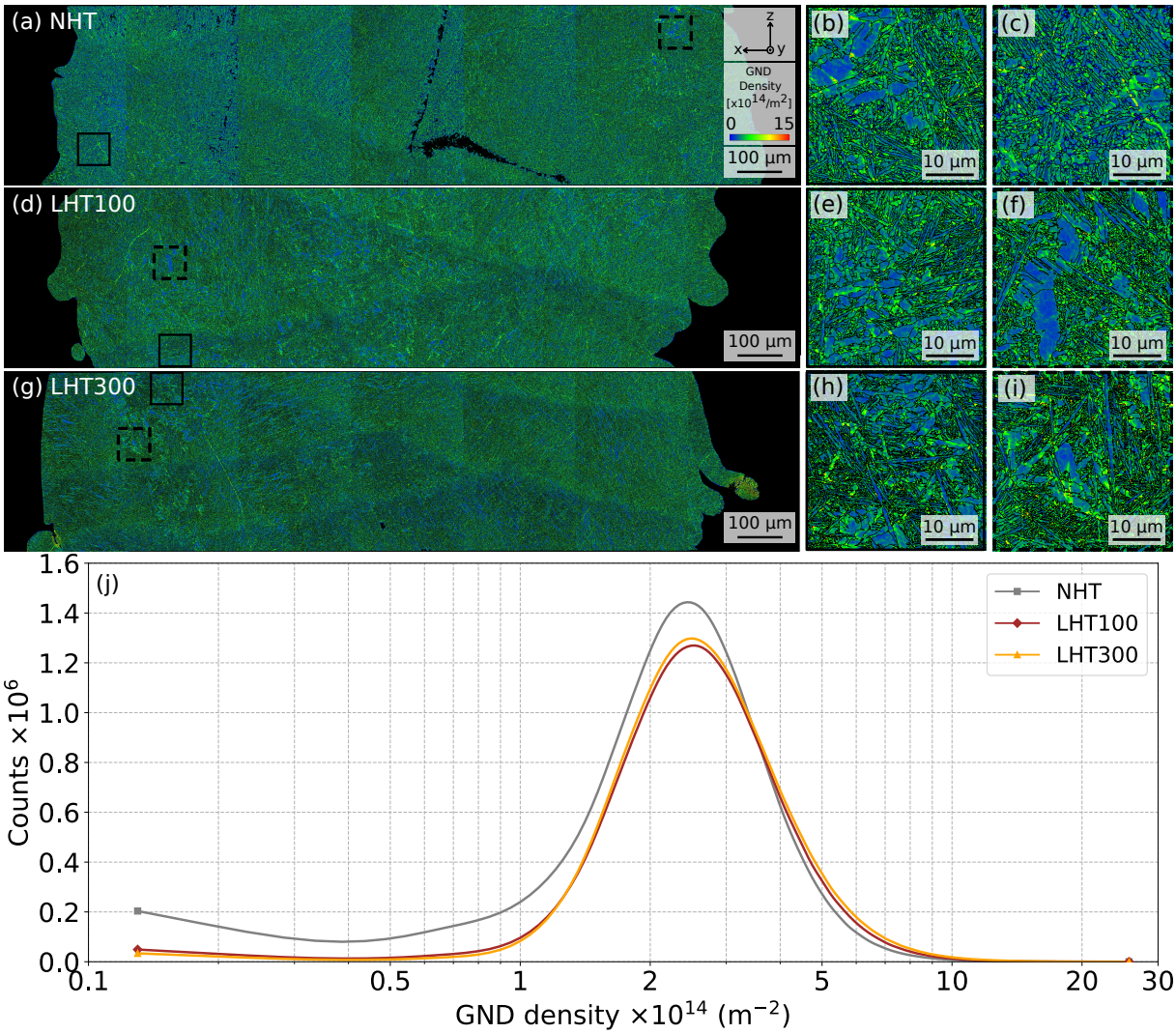

Figure 11: (a, d, and g) Geometrically necessary dislocation density maps, (b,c), (e,f) and (h,i) higher magnification views along with (j) distribution functions of NHT, LHT100, and LHT300.

3.5 Crystallographic texture

The averaged Debye-Scherrer rings representative of each sample that are presented in Figure 3a-c were analysed to deduce the presence of any predominant crystallographic orientation. For all samples, the rings are found to be continuous without any specific regions with high intensities, which implies similar texture between NHT, LHT100, and LHT300. Given the resemblance in diffraction patterns across samples, it can be deduced that crystallographic texture does not play a significant role in the differences observed in mechanical response between samples as reported in Figure 4a and b. This similarity also shows that the additional LHTs do not have a significant effect on texture across the samples.

To further support this claim, the Debye-Scherrer rings were summed for each layer and integrated over the azimuthal angle to obtain I vs. 2θ line profiles, and then averaged over a set of 7 adjacent layers in the region where the dogbones were extracted; this procedure is representative of the thickness of the gauge area of the dogbones. Then, the ratio of each diffration peak from the obtained normalised I vs. 2θ line profiles with respect to the corresponding one from the simulated line profiles for random textured

Ti-6Al-4V was calculated using Equation 1 and studied (see Table 4).

$$R = \left(\max I^{\text{exp}}_{(hkjl)_{\text{hcp}}} / \max I^{\text{exp}}_{(10\bar{1}1)_{\text{hcp}}}\right) / \left(\max I^{\text{sim}}_{(hkjl)_{\text{hcp}}} / \max I^{\text{sim}}_{(10\bar{1}1)_{\text{hcp}}}\right) \quad (1)$$

where R is the ratio between the considered experimental and simulated peak, $\max I^{\text{exp}}_{(hkjl)_{\text{hcp}}}$ and $\max I^{\text{exp}}_{(10\bar{1}1)_{\text{hcp}}}$ represent the maximum intensity of the experimental $(hkjl)_{\text{hcp}}$ and $(10\bar{1}1)_{\text{hcp}}$ peaks, respectively, and $\max I^{\text{sim}}_{(hkjl)_{\text{hcp}}}$, $\max I^{\text{sim}}_{(10\bar{1}1)_{\text{hcp}}}$ represents the maximum intensity of the simulated $(hkjl)_{\text{hcp}}$ and $(10\bar{1}1)_{\text{hcp}}$ peaks, respectively. For each identified peak (Figure 3d), the the R values are nearly identical across NHT, LHT100, and LHT300, indicating that crystallographic texture does not play a significant role in the difference in mechanical response between these samples.

Table 4: R values for the 9 hcp diffration peaks for NHT, LHT100, and LHT300. Peak 5 has contribution from $(1013)_{\text{hcp}}$ and from $(211)_{\text{bcc}}$.

	$(10\bar{1}0)_{\text{hcp}}$	$(0002)_{\text{hcp}}$	$(10\bar{1}2)_{\text{hcp}}$	$(10\bar{2}0)_{\text{hcp}}$	
NHT	0.95	1.06	0.97	0.99	
LHT100	0.91	1.24	0.80	0.65	
LHT300	0.97	0.96	1.27	1.06	
	$(1013)_{\text{hcp}}$ + $(211)_{\text{bcc}}$	$(11\bar{2}2)_{\text{hcp}}$	$(20\bar{2}0)_{\text{hcp}}$	$(20\bar{2}1)_{\text{hcp}}$	$(0004)_{\text{hcp}}$
NHT	0.99	0.91	0.87	0.87	0.94
LHT100	0.82	0.89	0.80	0.83	1.03
LHT300	1.03	0.92	0.86	0.80	0.88

4 Discussion

Collecting all the evidence from synchrotron XRD and microstructure analyses performed in Sections 3.2 - 3.5, the low phase fractions of α_m and the similarity in β fractions, intergranular lattice strains, crystallite/grain sizes, intragranular lattice strains, geometrically necessary dislocation densities and texture between samples should have a minor, if not negligible, contribution to the variation in the mechanical response between them. Thus, by elimination, the possibilities are narrowed down to the fractions of α' and α_d (see Figure 8), and the solid solution, which has not yet been addressed.

The differences in phase fractions of α' and α_d, highlighted in Figure 8, are directly related to the wide range of heating and cooling rates encountered during the process. The microstructure and internal strains just after deposition/solidification are not the same as those obtained at the end of the process. In other words, the solid-state thermal cycling experienced by a material due to subsequent layer addition or LHTs alters the fraction of phases that formed just after solidification. This alteration can occur in two ways: (i) The temperature of the material increases above the β transus resulting in complete re-transformation of all hcp phases into β; this change can occur in the initial stages of thermal cycling. In this case, a new set of hcp phases is formed during the subsequent cool down. (ii) The temperature does not increase above the β transus, which happens after a few thermal cycles and until the end of the process. In this case, thermal cycling triggers the diffusive decomposition of the metastable α' into α_d and β phases [17,57,60].

This diffusion-driven phenomenon and the degree of decomposition of α' are highly dependent on the local chemical composition (solid solution) and the time and temperature at which the heat treatment is performed. Cao et al. [61] investigated the degree of martensitic decomposition in annealed LPBF Ti-6Al-4V and the impact of annealing on the tensile properties. They reported a full decomposition of α' into fine α_d and β after annealing for at least six hours at 800°C. With this treatment, they were able to reach a YS and UTS of 937 MPa and 1041 MPa, respectively, with an elongation close to 18.5%. Note that in other works [62–64] annealing of LPBF Ti-6Al-4V is typically performed for 2h at 800°C to obtain a full decomposition of α'. Meanwhile, de Formanoir et al. [38] reportedly achieved a complete decomposition of α' in their EPBF Ti-6Al-4V after only 5 minutes of annealing at 700°C. This clearly demonstrates the influence of the process parameters on the microstructure formation, in particular the redistribution of solute atoms during fabrication. In the case of LPBF, the solid solution is much higher than in EPBF or LDED Ti-6Al-4V, and thus requires more time at high temperatures to decompose. Note that while it is possible to estimate the temperature occurring during the building and LHTs via X-ray diffraction measurements [65, 66], obtaining the local chemical composition is a very difficult, if not impossible, task. Therefore, it is difficult to know *a priori* how much time would be needed to fully decompose α'.

During LDED and LHTs of our Ti-6Al-4V, even though temperatures in the range $700 - 800$°C are not maintained for a very long time at any material point, evidence of significant (but not complete) decomposition of α' is clear in Figures 7 where α' needles coexist with α_m and lathy and globular α_d, as well as in Figure 8 where the proportions of α_d are higher than those of α' for all samples. Samples that underwent more thermal cycling (i.e., LHT100 and LHT300) with respect to NHT exhibited a higher degree of martensitic decomposition, with the highest amount of α_d. Interestingly, the amount of β phase remains the same between samples. As the number of thermal cycles decrease along BD, it is expected that the top of each sample present the least (if any) martensite decomposition [17, 24, 57].

A mechanism behind α' decomposition into α_d and β was recently proposed by Kaschel et al. [67]. Based on their analysis, the α' unit cell is initially in a compressed state. Upon heating the material from room temperature to 400°C, the a and c lattice parameters associated with α' slightly increase due to the redistribution of Al and V atoms yielding an undeformed martensite phase. Further heating causes a linear increase in a and c and the solute atoms, in particular V, diffuse out of the grain as α_d and β form out of α' at ~ 550°C. The diffusion of Al and V and substitution by Ti results in an unsymmetrical lattice due to varying chemical compositions, and an independent increase in basal and prismatic planes. The rate of diffusion increases with increasing temperature until the lattice is saturated in Ti. This saturation is accompanied by an expansion in the lattice size due to the larger size of Ti. This additional expansion provides sufficient room within the unit cell for elements to rearrange leading to full decomposition of α' into α_d and β. This full decomposition was observed to occur at 700°C and increasing the temperature beyond this point but below the β transus (995°C) simply accelerates the decomposition process. Note that these temperature values may not correspond exactly to the ones experienced by the Ti-6Al-4V studied in this work because the heating rate (200°C/min) used in the work of Kaschel et al. [67] is lower than the ones experienced during our LDED process. Also, the higher cooling/heating rates should result in lower decomposition due to less time at high temperatures.

As mentioned earlier, the variation in the number of thermal cycles that each layer experiences as a function of the BD also affects the chemical composition as a function of

sample height. Such a gradient in chemical composition has a direct consequence on the material strength through the change in solid solution. In particular, in the case of Ti-6Al-4V, addition of layers and LHTs result in the evaporation of Al [64,68,69]. Elemental composition analysis carried out on the NHT sample revealed a noticeable decrease in the Al wt% from 6.13 (powder) to 5.73 (see Section 2.1). Additional LHTs would result in a further decrease in Al content. In particular, LHT300 should result in more evaporation of Al than LHT100; chemical composition analysis could not be carried out on these samples due to lack of sufficient material. It is well known that the evaporation of Al reduces the solid solution strength [64,68,69]. Obtaining the precise contribution of this aspect to the overall mechanical response requires performing local mechanical tests such as nanoindentation all along the height of the sample and in multiple locations, which was beyond the scope of this work. Despite the additional Al evaporation that LHT100 would experience with respect to NHT, it should be noted that the former shows a better strength/ductility trade-off than the latter as well as nearly the same YS and UTS along PD. Therefore, it can be concluded that the differences in α_d and α' between samples has a much more important contribution to variation in mechanical response than the differences in Al content.

A reduction in Al content also results in an increase in the weight percent of other elements including the β stabilizing element V. The change in composition then also causes a change in the β transus and martensite start temperatures that can affect the hcp phase content. According to Zhang et al. [70], for Ti-alloys, a decrease in the α stabilizing elements such as Al results in a decrease in the β transus and martensite start temperature. Furthermore, an increase in β stabilizers such as V, results in further decrease in these temperatures. These differences between samples further contribute to the differences in the hcp phases that form. A clearer understanding of the change in chemical composition as a function of height would lead to a better understanding of the phase fractions formed and their impact on the mechanical response.

The heating and cooling rates encountered during LDED and LHTs also led to the occurrence of the α_m phase and its presence was higher in LHT100 than in NHT and LHT300. This phase also presented a much lower GND density than α' and α_d phases. Furthermore, in contrast to recent studies [28–32], in the present study this phase did not decompose into ultra-fine α_d and β lamellae as evidenced from the lack of structuring within this phase in the BSE images (Figure 7). For instance, Suprobo et al. [29] performed annealing at 850°C during 30 min to reach such a stage of decomposition of α_m. Karimi et al. [32] used a secondary laser during printing which lead to the decomposition of α_m. This phase has been reported to have a lower strength and higher ductility than α' and increasing its fraction could improve the strength-ductility trade-off. However, despite the fact that a lower fraction of α_m is present in LHT300, this sample exhibited a much higher ductility/toughness than NHT and LHT100, indicating that α' and α_d phases and the variation in the solid solution are playing the most important role in determining the differences in the mechanical response between samples.

5 Conclusion

In this work, the impact of in-process laser heat treatments (LHTs) on altering the microstructure and the mechanical response of laser direct energy deposited (LDED) Ti-6Al-4V is studied. The reference as-built sample is manufactured with a laser power of 300 W and two other samples are prepared with LHTs performed after the deposition of each

layer at 100 W (LHT100) and 300 W (LHT300). Uniaxial tensile test response is studied along the building and printing directions. All samples exhibit the same Young's moduli indicating that printing and additional LHTs result in at least a transversely isotropic elastic response in the plane formed by the building and printing directions. However, LHT100 exhibits a better strength/ductility trade-off than NHT. While LHT300 exhibits a poorer strength than both NHT and LHT100, a significant improvement in ductility and toughness is obtained. These alterations in the mechanical response are obtained simply from the LHTs and without any *in situ* alloying or post-process heat treatments.

Synchrotron XRD and electron microscopy measurements were performed prior to the extraction of dogbones to understand the contribution of different microstructural features and internal strains to the variations in mechanical response. The analysis reveals a similarity in the β phase fraction, intergranular lattice strains, grain sizes, intragranular lattice strains, geometrically necessary dislocation densities and texture between the samples. These features have a minor, if not negligible, contribution to the variation in the mechanical response between samples. Additional LHTs also result in the evaporation of Al, and a change in the solid solution strengthening effect. However, this difference is argued to have a negligible role due to the similarity in strength along the printing direction between NHT and LHT100. The only remaining possibility is then the difference in the hcp phase content between samples.

Among the different possible hcp phases, variations in the stable diffusively formed α_d (soft) and the metastable martensitic α' (hard) between samples are found to have a primary contribution to the difference in mechanical properties. LHT300 and NHT exhibit respectively the highest and lowest amount of α_d and the inverse for α', which explains the observed differences in mechanical properties. Another hcp phase, massive-α (α_m), also occurs in all samples but its proportion is an order of magnitude lower than α' and α_d. Nevertheless, its presence is the highest in LHT100 and along with its intermediate α' and α_d content, it contributes to a better strength/ductility trade-off than NHT.

This study highlights the tremendous potential of in-process LHTs in engineering the microstructure of LDED Ti-6Al-4V during manufacturing while exhibiting a good strength/ductility trade-off as well as improving ductility and toughness without the need of performing additional heat treatments outside an AM machine. In this sense, performing in-process LHTs can be further explored as a replacement for traditional post-process heat treatments such as annealing that incur an additional step outside the AM machine.

Acknowledgments

The authors acknowledge the support of the European Synchrotron Radiation Facility (ESRF) for beamtime access via proposal no. MA-5222 and thank Florian Russello for assistance and support in using beamline ID31. The authors also thank Hugo Pinsard in helping conducting the experiments. The authors are grateful to Phillipe Lasson and Ihssan Hendi from Synergie 4 for the EDS maps using their Flatquad detector (Brucker). The authors thank Kewei Chen, Alexandre Tanguy, Nathalie Isaac and Kassiogé Dembélé for the support during experimental characterization. The authors would also like to thank Sandrine Tuseau-Nenez, Kim Vanmeensel and Pushkar Prakash Dhekne for the fruitful discussions on the XRD data. KAA, SG and MVU are grateful to European Research Council (ERC) for their support through the European Union's Horizon 2020 research and innovation program for Starting Grant project GAMMA (Grant agreement ID: 946959).

Funding

This work was supported by the Horizon 2020 - EXCELLENT SCIENCE - European Research Council Starting Grant 2020 project GAMMA (Grant agreement ID: 946959).

Declaration of competing interest

The authors declare no conflict of interest. The funders had no role in the design of the study, collection, analyses, and interpretation of data in the writing of the manuscript, or in the decision to publish the results.

Data availability

Data will be made available on request. Open access to synchrotron experimental raw data will be available on July 2025, see https://doi.org/10.15151/ESRF-ES-847864546

References

[1] M. J. Donachie, Titanium: a technical guide. Materials Park, OH: ASM International, 2nd ed ed., 2000.

[2] C. Leyens and M. Peters, eds., Titanium and Titanium Alloys: Fundamentals and Applications. Wiley, 1 ed., July 2003.

[3] Z. Liu, B. He, T. Lyu, and Y. Zou, "A Review on Additive Manufacturing of Titanium Alloys for Aerospace Applications: Directed Energy Deposition and Beyond Ti-6Al-4V," JOM, vol. 73, Apr. 2021.

[4] F. A. Shah, A. Snis, A. Matic, P. Thomsen, and A. Palmquist, "3D printed Ti6Al4V implant surface promotes bone maturation and retains a higher density of less aged osteocytes at the bone-implant interface," Acta Biomaterialia, vol. 30, pp. 357–367, Jan. 2016.

[5] G. Welsch, R. Boyer, and E. W. Collings, Materials Properties Handbook: Titanium Alloys. ASM International, Dec. 1993. Google-Books-ID: Oke6AQAACAAJ.

[6] T. DebRoy, H. Wei, J. Zuback, T. Mukherjee, J. Elmer, J. Milewski, A. Beese, A. Wilson-Heid, A. De, and W. Zhang, "Additive manufacturing of metallic components – Process, structure and properties," Progress in Materials Science, vol. 92, pp. 112–224, Mar. 2018.

[7] B. Dutta and F. H. S. Froes, "The Additive Manufacturing (AM) of titanium alloys," Metal Powder Report, vol. 72, pp. 96–106, Mar. 2017.

[8] S. Alipour, A. Moridi, F. Liou, and A. Emdadi, "The Trajectory of Additively Manufactured Titanium Alloys with Superior Mechanical Properties and Engineered Microstructures," Additive Manufacturing, vol. 60, p. 103245, Dec. 2022.

[9] S. Gorsse, C. Hutchinson, M. Gouné, and R. Banerjee, "Additive manufacturing of metals: a brief review of the characteristic microstructures and properties of steels, Ti-6Al-4V and high-entropy alloys," Science and Technology of Advanced Materials, vol. 18, pp. 584–610, Dec. 2017. Publisher: Taylor & Francis _eprint: https://doi.org/10.1080/14686996.2017.1361305.

[10] S.-O. Agbedor, H. Wu, Y. Ren, L. Liang, D. Yang, B. Liu, Y. Liu, and I. Baker, "A two-decade odyssey in fusion-based additive manufacturing of titanium alloys and composites," Applied Materials Today, vol. 39, p. 102242, Aug. 2024.

[11] I. Gibson, D. Rosen, B. Stucker, and M. Khorasani, Additive Manufacturing Technologies. Cham: Springer International Publishing, 2021.

[12] D. Herzog, V. Seyda, E. Wycisk, and C. Emmelmann, "Additive manufacturing of metals," Acta Materialia, vol. 117, pp. 371–392, Sept. 2016.

[13] H. D. Nguyen, A. Pramanik, A. K. Basak, Y. Dong, C. Prakash, S. Debnath, S. Shankar, I. S. Jawahir, S. Dixit, and D. Buddhi, "A critical review on additive manufacturing of Ti-6Al-4V alloy: microstructure and mechanical properties," Journal of Materials Research and Technology, vol. 18, pp. 4641–4661, May 2022.

[14] B. Vrancken, L. Thijs, J. P. Kruth, and J. Van Humbeeck, "Microstructure and mechanical properties of a novel β titanium metallic composite by selective laser melting," Acta Materialia, vol. 68, pp. 150–158, Apr. 2014.

[15] P. Peyre and E. Charkaluk, Additive Manufacturing of Metal Alloys 2: Microstructures, Post-processing and Use Properties. John Wiley & Sons, 2023.

[16] D. A. Porter, K. E. Easterling, and M. Y. Sherif, Phase Transformations in Metals and Alloys. Boca Raton: CRC Press, 4 ed., Nov. 2021.

[17] J. Maisonneuve, Fabrication directe de pièces aéronautiques en TA6V et IN718 : projection et fusion sélective par laser. These de doctorat, Paris, ENMP, Jan. 2008.

[18] T. Blanc, Fabrication additive par dépôt laser direct de TA6V : étude expérimentale dans des régimes de forte productivité, modèles de comportement et recyclage de la poudre. These de doctorat, Paris Sciences et Lettres (ComUE), Apr. 2017.

[19] S. Banerjee and P. Mukhopadhyay, Phase Transformations: Examples from Titanium and Zirconium Alloys. Elsevier, May 2010. Google-Books-ID: 46ECHriRKkUC.

[20] G. Lütjering and J. C. Williams, Titanium. Engineering Materials, Processes, Berlin, Heidelberg: Springer, 2007.

[21] S. A. Oh, J. W. Aroh, N. L. Lamprinakos, C. A. Chuang, A. N. Bucsek, and A. D. Rollett, "Martensite decomposition during rapid heating of Ti-6Al-4V studied via in situ synchrotron X-ray diffraction," Communications Materials, vol. 5, pp. 1–10, Apr. 2024. Publisher: Nature Publishing Group.

[22] T. Ahmed and H. J. Rack, "Phase transformations during cooling in $\alpha + \beta$ titanium alloys," Materials Science and Engineering: A, vol. 243, pp. 206–211, Mar. 1998.

[23] H. Y. Ma, J. C. Wang, P. Qin, Y. J. Liu, L. Y. Chen, L. Q. Wang, and L. C. Zhang, "Advances in additively manufactured titanium alloys by powder bed fusion and directed energy deposition: Microstructure, defects, and mechanical behavior," Journal of Materials Science & Technology, vol. 183, pp. 32–62, June 2024.

[24] S. M. Kelly and S. L. Kampe, "Microstructural evolution in laser-deposited multilayer Ti-6Al-4V builds: Part I. Microstructural characterization," Metallurgical and Materials Transactions A, vol. 35, pp. 1861–1867, June 2004.

[25] T. B. Massalski, "Massive transformations revisited," Metallurgical and Materials Transactions A, vol. 33, pp. 2277–2283, Aug. 2002.

[26] M. Perricone, "Massive Transformation Structures," in Metallography and Microstructures (G. F. Vander Voort, ed.), pp. 148–151, ASM International, Dec. 2004.

[27] D. Nursyifaulkhair, N. Park, E. R. Baek, and S. Kim, "Influence of cooling rate on volume fraction of α massive phase in a Ti-6Al-4V alloy fabricated using directed energy deposition," Materials Letters, vol. 257, p. 126671, Dec. 2019.

[28] S. L. Lu, M. Qian, H. P. Tang, M. Yan, J. Wang, and D. H. StJohn, "Massive transformation in Ti–6Al–4V additively manufactured by selective electron beam melting," Acta Materialia, vol. 104, pp. 303–311, Feb. 2016.

[29] G. Suprobo, A. A. Ammar, N. Park, E. R. Baek, and S. Kim, "Thermal Decomposition of Massive Phase to Fine Lamellar α/β in Ti–6Al–4V Additively Manufactured Alloy by Directed Energy Deposition," Metals and Materials International, vol. 25, pp. 1428–1435, Nov. 2019.

[30] E. R. Baek and G. Suprobo, "Massive Phase Transformation as a New Prospective on Microstructural Design in a Titanium Alloy - A Review," Materials Science Forum, vol. 1000, pp. 428–435, 2020. Conference Name: The 16th Quality in Research International Symposium on Metallurgy & Materials Engineering Publisher: Trans Tech Publications Ltd.

[31] S. L. Lu, D. Han, D. Y. Qin, T. Song, D. Qiu, M. Brandt, H. P. Tang, and M. Qian, "Massive transformations in titanium alloys: Role of relative orientation of adjacent parent grains," Scripta Materialia, vol. 239, p. 115776, Jan. 2024.

[32] J. Karimi, C. Zhao, and K. G. Prashanth, "Massive transformation in dual-laser powder bed fusion of Ti6Al4V alloys," Journal of Manufacturing Processes, vol. 119, pp. 282–292, June 2024.

[33] M. Ahlfors, "Hot Isostatic Pressing for Metal Additive Manufacturing," in Additive Manufacturing Processes, ASM International, 06 2020.

[34] S. Cao, Y. Zou, C. V. S. Lim, and X. Wu, "Review of laser powder bed fusion (LPBF) fabricated Ti-6Al-4V: process, post-process treatment, microstructure, and property," Light: Advanced Manufacturing, vol. 2, pp. 313–332, Sept. 2021. Publisher: Light: Advanced Manufacturing.

[35] T. Vilaro, C. Colin, and J. D. Bartout, "As-Fabricated and Heat-Treated Microstructures of the Ti-6Al-4V Alloy Processed by Selective Laser Melting," Metallurgical and Materials Transactions A, vol. 42, pp. 3190–3199, Oct. 2011.

[36] R. Sabban, S. Bahl, K. Chatterjee, and S. Suwas, "Globularization using heat treatment in additively manufactured Ti-6Al-4V for high strength and toughness," Acta Materialia, vol. 162, pp. 239–254, Jan. 2019.

[37] C.-L. Li, J.-K. Hong, P. L. Narayana, S.-W. Choi, S. W. Lee, C. H. Park, J.-T. Yeom, and Q. Mei, "Realizing superior ductility of selective laser melted Ti-6Al-4V through a multi-step heat treatment," Materials Science and Engineering: A, vol. 799, p. 140367, Jan. 2021.

[38] C. De Formanoir, A. Brulard, S. Vivès, G. Martin, F. Prima, S. Michotte, E. Rivière, A. Dolimont, and S. Godet, "A strategy to improve the work-hardening behavior of Ti–6Al–4V parts produced by additive manufacturing," Materials Research Letters, vol. 5, pp. 201–208, May 2017.

[39] R. Esmaeilzadeh, M. Hamidi-Nasab, C. de Formanoir, L. Schlenger, S. Van Petegem, C. Navarre, C. Cayron, N. Casati, D. Grolimund, and R. E. Logé, "*In-situ* selective laser heat treatment for microstructural control of additively manufactured Ti-6Al-4V," Additive Manufacturing, vol. 78, p. 103882, Sept. 2023.

[40] C. J. Rietema, J. D. Roehling, W. L. Smith, and K. M. Bertsch, "Microstructural control of additively manufactured Ti6Al4V via *in-situ* large-area laser annealing," Scripta Materialia, vol. 239, p. 115823, Jan. 2024.

[41] X. Chen and C. Qiu, "In-situ development of a sandwich microstructure with enhanced ductility by laser reheating of a laser melted titanium alloy," Scientific Reports, vol. 10, p. 15870, Sept. 2020. Publisher: Nature Publishing Group.

[42] S. Gaudez, K. A. Abdesselam, H. Gharbi, Z. Hegedüs, U. Lienert, W. Pantleon, and M. V. Upadhyay, "High-resolution reciprocal space mapping reveals dislocation structure evolution during 3D printing," Additive Manufacturing, vol. 71, p. 103602, June 2023.

[43] J. Kieffer and G. Ashiotis, "PyFAI: a Python library for high performance azimuthal integration on GPU," arXiv:1412.6367 [astro-ph], Dec. 2014. arXiv: 1412.6367.

[44] H. M. Rietveld, "A profile refinement method for nuclear and magnetic structures," Journal of Applied Crystallography, vol. 2, pp. 65–71, June 1969. Publisher: International Union of Crystallography.

[45] J. Rodríguez-Carvajal, "Recent advances in magnetic structure determination by neutron powder diffraction," Physica B: Condensed Matter, vol. 192, pp. 55–69, Oct. 1993.

[46] S. Gražulis, A. Daškevič, A. Merkys, D. Chateigner, L. Lutterotti, M. Quirós, N. R. Serebryanaya, P. Moeck, R. T. Downs, and A. Le Bail, "Crystallography Open Database (COD): an open-access collection of crystal structures and platform for world-wide collaboration," Nucleic Acids Research, vol. 40, pp. D420–D427, Jan. 2012.

[47] B. H. Toby, "R factors in Rietveld analysis: How good is good enough?," Powder Diffraction, vol. 21, pp. 67–70, Mar. 2006.

[48] L. B. McCusker, R. B. Von Dreele, D. E. Cox, D. Louër, and P. Scardi, "Rietveld refinement guidelines," Journal of Applied Crystallography, vol. 32, pp. 36–50, Feb. 1999.

[49] C. Suryanarayana and M. G. Norton, "Crystal Structure Determination. II: Hexagonal Structures," in X-Ray Diffraction, pp. 125–152, Boston, MA: Springer US, 1998.

[50] J. Schindelin, I. Arganda-Carreras, E. Frise, V. Kaynig, M. Longair, T. Pietzsch, S. Preibisch, C. Rueden, S. Saalfeld, B. Schmid, J.-Y. Tinevez, D. J. White, V. Hartenstein, K. Eliceiri, P. Tomancak, and A. Cardona, "Fiji: an open-source

platform for biological-image analysis," Nature Methods, vol. 9, pp. 676–682, July 2012. Publisher: Nature Publishing Group.

[51] S. Preibisch, S. Saalfeld, and P. Tomancak, "Globally optimal stitching of tiled 3D microscopic image acquisitions," Bioinformatics, vol. 25, pp. 1463–1465, June 2009.

[52] G. P. Grabovetskaya, E. N. Melnikova, Y. R. Kolobov, I. P. Chernov, E. V. Naidenkin, N. N. Nikitenkov, and I. P. Mishin, "Evolution of the structural and phase states of a Ti-6Al-4V alloy in forming submicrocrystalline structure with the use of temporary hydrogenation," Russian Physics Journal, vol. 49, pp. 442–447, Apr. 2006.

[53] L. Thijs, F. Verhaeghe, T. Craeghs, J. V. Humbeeck, and J.-P. Kruth, "A study of the microstructural evolution during selective laser melting of Ti–6Al–4V," Acta Materialia, vol. 58, pp. 3303–3312, May 2010.

[54] J. Yang, H. Yu, J. Yin, M. Gao, Z. Wang, and X. Zeng, "Formation and control of martensite in Ti-6Al-4V alloy produced by selective laser melting," Materials & Design, vol. 108, pp. 308–318, Oct. 2016.

[55] I. Gibson, D. Rosen, and B. Stucker, "Directed Energy Deposition Processes," in Additive Manufacturing Technologies: 3D Printing, Rapid Prototyping, and Direct Digital Manufacturing (I. Gibson, D. Rosen, and B. Stucker, eds.), pp. 245–268, New York, NY: Springer, 2015.

[56] D.-G. Ahn, "Directed Energy Deposition (DED) Process: State of the Art," International Journal of Precision Engineering and Manufacturing-Green Technology, vol. 8, pp. 703–742, Mar. 2021.

[57] A. Zafari, M. R. Barati, and K. Xia, "Controlling martensitic decomposition during selective laser melting to achieve best ductility in high strength Ti-6Al-4V," Materials Science and Engineering: A, vol. 744, pp. 445–455, Jan. 2019.

[58] G. K. Williamson and W. H. Hall, "X-ray line broadening from files aluminium and wolfram," Acta Metallurgica, vol. 1, pp. 22–31, 1953.

[59] Y. Chong, G. Deng, S. Gao, J. Yi, A. Shibata, and N. Tsuji, "Yielding nature and Hall-Petch relationships in Ti-6Al-4V alloy with fully equiaxed and bimodal microstructures," Scripta Materialia, vol. 172, pp. 77–82, Nov. 2019.

[60] W. Xu, M. Brandt, S. Sun, J. Elambasseril, Q. Liu, K. Latham, K. Xia, and M. Qian, "Additive manufacturing of strong and ductile Ti–6Al–4V by selective laser melting via in situ martensite decomposition," Acta Materialia, vol. 85, pp. 74–84, Feb. 2015.

[61] S. Cao, R. Chu, X. Zhou, K. Yang, Q. Jia, C. V. S. Lim, A. Huang, and X. Wu, "Role of martensite decomposition in tensile properties of selective laser melted Ti-6Al-4V," Journal of Alloys and Compounds, vol. 744, pp. 357–363, May 2018.

[62] B. Vrancken, L. Thijs, J.-P. Kruth, and J. Van Humbeeck, "Heat treatment of Ti6Al4V produced by Selective Laser Melting: Microstructure and mechanical properties," Journal of Alloys and Compounds, vol. 541, pp. 177–185, Nov. 2012.

[63] S. Leuders, M. Thöne, A. Riemer, T. Niendorf, T. Tröster, H. A. Richard, and H. J. Maier, "On the mechanical behaviour of titanium alloy TiAl6V4 manufactured by selective laser melting: Fatigue resistance and crack growth performance," International Journal of Fatigue, vol. 48, pp. 300–307, Mar. 2013.

[64] E. Sallica-Leva, R. Caram, A. L. Jardini, and J. B. Fogagnolo, "Ductility improvement due to martensite α' decomposition in porous Ti–6Al–4V parts produced by selective laser melting for orthopedic implants," Journal of the Mechanical Behavior of Biomedical Materials, vol. 54, pp. 149–158, Feb. 2016.

[65] S. Hocine, H. Van Swygenhoven, S. Van Petegem, C. S. T. Chang, T. Maimaitiyili, G. Tinti, D. Ferreira Sanchez, D. Grolimund, and N. Casati, "Operando X-ray diffraction during laser 3D printing," Materials Today, vol. 34, pp. 30 – 40, Nov. 2019.

[66] P. P. Dhekne, M. Bönisch, M. Seefeldt, and K. Vanmeensel, "In-situ synchrotron X-ray diffraction investigation of martensite decomposition in Laser Powder Bed Fusion (L-PBF) processed Ti–6Al–4V," Materials Science and Engineering: A, vol. 899, p. 146421, May 2024.

[67] F. R. Kaschel, R. K. Vijayaraghavan, A. Shmeliov, E. K. McCarthy, M. Canavan, P. J. McNally, D. P. Dowling, V. Nicolosi, and M. Celikin, "Mechanism of stress relaxation and phase transformation in additively manufactured Ti-6Al-4V via *in situ* high temperature XRD and TEM analyses," Acta Materialia, vol. 188, pp. 720–732, Apr. 2020.

[68] A. Azarniya, X. G. Colera, M. J. Mirzaali, S. Sovizi, F. Bartolomeu, M. St Weglowski, k, W. W. Wits, C. Y. Yap, J. Ahn, G. Miranda, F. S. Silva, H. R. Madaah Hosseini, S. Ramakrishna, and A. A. Zadpoor, "Additive manufacturing of Ti–6Al–4V parts through laser metal deposition (LMD): Process, microstructure, and mechanical properties," Journal of Alloys and Compounds, vol. 804, pp. 163–191, Oct. 2019.

[69] S. Zhao, R. Zhang, Q. Yu, J. Ell, R. O. Ritchie, and A. M. Minor, "Cryoforged nanotwinned titanium with ultrahigh strength and ductility," Science, vol. 373, pp. 1363–1368, Sept. 2021. Publisher: American Association for the Advancement of Science.

[70] J. Zhang, H. Guo, M. Hu, H. Xu, H. Ju, D. Xu, C. Teng, and R. Yang, "Effect of common alloying elements on α' martensite start temperature in titanium alloys," Journal of Materials Research and Technology, vol. 27, pp. 4562–4572, Nov. 2023.